Polymer 50 (2009) 4644–4655

Contents lists available at ScienceDirect

Polymer

journal homepage: www.elsevier.com/locate/polymer

Real time mechano-optical study on deformation behavior of PTMO/CHDI-based polyetherurethanes under uniaxial extension

E. Unsal [a,b], B. Yalcin [a], I. Yilgor [b], E. Yilgor [b], M. Cakmak [a,*]

[a] Department of Polymer Engineering, University of Akron, Akron, OH 44325-0301, USA
[b] Department of Chemistry, Koc University, Sariyer, 34450 Istanbul, Turkey

ARTICLE INFO

Article history:
Received 3 June 2009
Received in revised form
17 July 2009
Accepted 26 July 2009
Available online 29 July 2009

Keywords:
Polyurethanes
Strain optical
Stress optical behavior

ABSTRACT

Real time mechano-optical properties of two homologous segmented, thermoplastic polyurethanes (TPUs) obtained from the stoichiometric reactions of trans-1,4-cyclohexyl diisocyanate (CHDI) and poly(tetramethylene oxide)glycol (PTMO) were investigated. PTMO oligomers used had number average molecular weights $\langle M_n \rangle$ of 1020 and 2040 g/mol, resulting in TPUs with urethane hard segment contents of 14 and 7.5% by weight. AFM studies showed intertwined microphase morphology. Stress–strain measurements demonstrated the formation of very strong, elastomeric materials, with ultimate tensile strengths of 23–25 MPa and elongation at break values of about 1000%. Mechano-optical behavior of these polymers exhibited multiple regime behavior. The first strain optical regime is linear where primarily the soft segments orient. The transition between the first and second strain optical regimes was found to correspond to the saturation of straining of the soft segments that lead to start of rotation of hard segments in the stretching direction. The start of Regime II coincides with the onset of strain hardening and the distance between the hard segments increases appreciably with stretching in this regime. Increasing the soft segment length was found to promote its strain-induced crystallization.

1. Introduction

Thermoplastic polyurethanes (TPUs) [1,2] represent a subcategory of thermoplastic elastomers (TPEs) that can be tailored to display a wide range of properties particularly suited for many emerging fields, such as biomaterials, tissue engineering [3–5], optoelectronics [6], shape-memory materials [7,8], conducting polymers [9], molecular recognition [10], smart surfaces and others [11,12]. Versatility of TPU technology stems from the commercial availability of a very large number of starting materials for their synthesis. TPUs consist of alternating soft and hard segments, chemically linked to each other along a polymer backbone. In the solid state, soft and hard segments aggregate into their respective phases resulting in microphase separated morphology. Overall properties and performance of TPUs strongly depend on their microphase morphologies, which generally consist of domains of hard segments distributed in a continuous matrix of the soft segments. Although there are a large number of factors that influence the microphase separation in TPUs [2,13,14], the primary ones are: (i) solubility parameter difference between hard and soft segments,(ii) the strength and extent of hydrogen bonding between urethane hard segments and (ii) the symmetry of the hard segments [15].

Conventionally, the TPUs are prepared by the reaction of an excess amount of diisocyanate with polyether or polyester glycols to form an isocyanate terminated prepolymer [13,14]. This is followed by the chain extension of the prepolymer with stoichiometric amounts of a short-chain diol or diamine to form the hard segments and produce high molecular weight TPUs [13,14]. The use of short-chain diols such as 1-4 butanediol (BDO) results in the formation of polyurethanes (PU) while the short-chain aliphatic diamine chain extenders such as ethylene diamine (ED) produce poly(urethane–urea) (PUU). PUs can typically be processed thermally whereas PUUs are in most cases only suitable for processing from solution due to the presence of hard segments with very strong polar functionalities. Very recently, it has been demonstrated that segmented PUs and PUUs that display a microphase morphology and attractive elastomeric properties, such as high modulus, tensile strength and excellent elongation to break, can also be prepared in a one step process through the stoichiometric reactions between diisocyanates and poly(tetramethylene oxide)-glycol (PTMO) oligomers *without using any chain extenders* [16–20]. The resulting microphase morphologies and properties of these novel TPUs are strongly dependent on the type of the hard segments formed (urethane or urea) and the symmetry of the diisocyanate used [16–20]. Such TPUs typically possess very low-hard

* Corresponding author.
E-mail address: cakmak1@uakron.edu (M. Cakmak).

0032-3861/$ – see front matter © 2009 Elsevier Ltd. All rights reserved.
doi:10.1016/j.polymer.2009.07.041

segment content limited by the stoichiometry of the reaction. Interestingly, however, they still display very strong mechanical properties. In a previous paper [17], Yilgor et al. of this study reported an urethane system with 14% hard segment content prepared through the stoichiometric reaction between trans-1,4-cyclohexyl diisocyanate (CHDI) and poly(tetramethylene oxide)-glycol (PTMO) without any chain extender exhibiting a modulus value of 50–70 MPa, tensile strength of 20–25 MPa and an elongation to break of 1000%. In addition, these PUs with low-hard segment content exhibit rubbery plateaus extending from −50° to 150 °C indicating that they can be used in various applications where conventional TPUs with 30–35% hard segments are used. In this paper, we use the same CHDI–PTMO urethane systems and study their microstructural mesophase deformation behavior under uniaxial extension at room temperature.

Structural development of polyurethanes during deformation is an important and well-researched area with publications dating back to 1960s. In the early 1960s, Rinke [21] and Oertel [22] described the chemistry and preparation of highly elastic polyurethane fibers and studied their structure in extended form by X-ray diffraction. In mid 1960s, Cooper and Tobolsky carried out temperature–modulus measurements on plasticizer loaded polyurethane sheets using torsional testing apparatus in order to identify the origin of enhanced modulus in these polymers [23]. They were among the first to associate the elastomeric properties of segmented polyurethanes to the phase separated morphology, especially the hard blocks acting as fillers for the soft phase. By the end of 1960s, the interest on the effect of mechanical deformation on the mesophase structure in segmented polyurethanes grew rapidly. Bonart carried out the first systematic WAXD and SAXS studies on the orientation of the periodic microphase structure under tensile deformation [24,25]. Cooper and coworkers reported studies on the temperature dependence of the stress–strain-birefringence behavior of polyurethanes [26,27] and measured the preferred orientation of the hard and soft segment molecular units within the microphases using infrared dichroism [28–30]. In the 1980s, Desper and Schneider have quantitatively characterized microphase segregation in polyurethanes in the undeformed state [31] using SAXS. Later on, they studied three different classes of polyurethanes in deformed state [32] and identified three different modes of microstructural deformation to occur in these uniaxially stretched polymers. The first class of polyurethanes, i.e. amine cured polyurethanes, exhibited hard segments tilting away from the stretching direction in a pool of shear deformed soft segments. This type of deformation was associated with a four-point SAXS pattern. Upon stretching, the diol cured polyurethanes showed the evolution of two-point SAXS patterns with hard segments orienting normal to the stretching direction while the soft segments deform in tension. The third class of polyurethanes, triol cured polyurethanes, on the other hand, were found to exhibit either rotation or translation of microparticles upon deformation.

Numerous other studies have been carried out to study the structural development during deformation of polyurethanes [33–37]. Recent structure development studies on the deformation behavior of polyurethanes typically combine multiple real time characterization techniques to reveal the complex mechanisms of hard–soft segment behavior during deformation. Yeh et al. for instance used in-situ wide angle X-ray diffraction and small angle X-ray scattering using synchrotron radiation as well as time-resolved Fourier transform infrared spectroscopy to investigate the segmental orientation of PUU elastomers containing 12-wt% hard segments during cyclic elongation and recovery real time [38]. Their results showed that the hard segment lamellar stacks without any preferred orientation initially tilted with respect to the stretching direction at strain levels between 50 and 150% leading to a four-point SAXS pattern. At higher strain levels, the four-point pattern transformed to a two-point pattern and was interpreted as breakdown of tilted lamellar stacks leading to the orientation of their domain in the stretching direction. An equatorial streak was also superimposed onto these two-point patterns which was attributed to scattering from nanofibrils of strain-induced soft segment crystals and broken down hard domains. In a similar study, Sauer et al. investigated the morphology and orientation during deformation of TPEs containing PTMO soft segments and nylon 12 hard segments (Pebax) via SAXS, AFM, birefringence and DSC [39]. Their 2D SAXS patterns also exhibited similar features as that of PUUs in Yeh et al.'s work [38]. Initially circular arc deformed into a flattened ellipse at 50% strain indicative of increased long spacing of lamellar hard domains while keeping the orientation fairly isotropic. At higher strains SAXS patterns had contributions from intra-nanofibril meridonial 2 point (correlation between hard and soft regions in the fibril) and inter-fibrillar equatorial scattering. The interpretations of SAXS patterns in their study were substantiated with AFM images of undeformed and deformed samples. In a study of simultaneous SAXS and force measurements during tensile load/unload deformation of two polyurethanes of identical chemistry but different block length distribution, i.e. monodisperse vs. randomized hard segments, Blundell et al. reported quite different initial morphologies, which deform distinctly in different ways [40,41]. Recently, the properties and morphology of segmented copoly(ether urea)s with uniform hard segments was also reported [20].

These studies clearly showed the importance of studying the phase morphology during stretching to identify the deformation, relaxation and possible failure mechanisms in these polymers.

With the exception of one previous work by us on PUU [42] (Polyurethane urea), real time stress and strain optical behavior of polyurethanes has not been investigated. The primary focus of our study is to investigate the dynamical evolution of structural development as reflected in real time stress and strain optical behavior during their uniaxial deformation. We accomplish this by using a unique stretching device that accurately tracks strain (true, Hencky) and true stress and spectral birefringence real time with millisecond data collection frequency. The details of mechanistic changes that are observed in real time mechano-optical measurements are then identified by offline AFM, SAXS, and WAXS studies on the films captured at the key deformation levels.

2. Experimental methods

2.1. Materials

Trans-1,4-cyclohexyl diisocyanate (CHDI) was purchased from DuPont and used as received. Poly(tetramethylene oxide) glycol oligomers with $\langle M_n \rangle$ values of 1020 (PTMO1k) and 2040 g/mol (PTMO-2k) were kindly provided by DuPont. Reagent grade tetrahydrofuran (THF) was purchased from Sigma–Aldrich, Inc. and used as received. Dibutyltin dilaurate (T-12) was a product of Air Products and Chemicals, Inc.

2.2. Polymer synthesis

Polymerization reactions were conducted in three-neck, round bottom, Pyrex reaction flasks equipped with an overhead stirrer, reflux column and nitrogen inlet. Copolymers were prepared by the reaction of equimolar amounts of diisocyanate and PTMO in THF at 60 °C. No chain extenders were utilized. In a typical polymerization reaction 1.66 g (10.0 mmol) of CHDI and 10.20 g of PTMO1k (10.0 mmol) were introduced into a 250 mL Pyrex reaction vessel and stirred. Clear mixture was heated to 60 °C and 100 ppm of T-12

catalyst in THF solution was added. As the molecular weight of the polymer formed increased with conversion, the reaction mixture was diluted with THF to keep the viscosity low for effective agitation. Completion of the reactions was determined by monitoring the disappearance of the strong isocyanate absorption peak around 2268 cm^{-1} by FTIR.

Chemical structures of the polyurethanes (coded as CHDI-1U and CHDI-2U) investigated in this study are provided in Fig. 1. Chemical compositions, hard segment contents and average molecular weights of polyurethanes obtained are provided in Table 1. SEC results clearly demonstrate the formation of high molecular weight polymers.

Polymer films with a thickness of approximately 1 mm were prepared by solvent casting into Teflon molds. The molds were covered with a glass Petri dish to slow down the solvent evaporation and kept at room temperature overnight. After evaporation of the solvent, the molds were placed in a vacuum oven at 60 °C for complete drying, which was monitored gravimetrically. The resulting films were then removed from the Teflon molds and stored in polyethylene bags at room temperature until testing.

2.3. Characterization methods

2.3.1. Fourier transform infrared (FTIR) spectroscopy

FTIR spectra were recorded on a Nicolet Impact 400D FTIR spectrometer. FTIR scans were collected on thin films (*ca.* 10 μ in thickness) cast on KBr discs from THF solution.

2.3.2. Size exclusion chromatography (SEC)

SEC measurements were conducted on a Waters system that was equipped with three in-line PLgel 5 mm Mixed-C columns, an autosampler, a 410 RI detector, a Viscotek 270 dual detector, and an in-line Wyatt Technologies miniDawn multiple angle laser light scattering (MALLS) detector. SEC measurements were performed at 50 °C in DMF with a flow rate of 1 mL/min. Absolute molecular weights were obtained from MALLS detector.

2.3.3. Differential scanning calorimetry (DSC) (thermal analysis)

DSC experiments were performed using TA Instruments, DSC Q2000. Software: Q Advantage, V 2.8.0.392. As-cast films were placed in aluminum sample holders and crimped. Before the start of thermal cycle, samples were heated from room temperature to 280 °C and kept for 5 min to erase thermal history. They were then cooled to cryogenic temperatures of −150 °C at 10 °C/min and subsequently heated to 280 °C at 10 °C/min to capture the entire cooling and heating profile between −150 °C and 280 °C.

2.3.4. Instrumentation of the uniaxial stretcher and mechano-optical behavior during stretching

The uniaxial stretching experiments were carried out using a custom built instrumented uniaxial stretching system shown in Fig. 2 that allows the real time determination of true stress, true strain, and birefringence simultaneously during stretching. Although the details of this stretching machine is given elsewhere [43,44], below we provide a brief overview. Online spectral birefringence is essentially based on the method described by Beekmans and Posthumna de Boer et al. [45]. In this method white light is used as the light source to get the order number of retardation automatically. To measure the birefringence, the thickness must be measured at the same time and at the same location where the birefringence is measured. This is accomplished by moving the two cross-heads of the stretching frame in opposing directions allowing the narrowest symmetry plane of the sample to remain spatially stationary. A laser micrometer mounted at 45° to the horizontal plane is focused at this stationary symmetry plane such that it continuously monitors the width of the sample during the course of stretching and holding stages. The temporal development of thickness and thus cross-sectional areas are then determined utilizing uniaxial symmetry and (Eq. (1)) with the knowledge of initial thickness and widths.

For elongation we consider three parameters, i.e. engineering strain, true strain and Hencky strain. Engineering strain is defined as the ratio of elongation (difference between the final length and the initial length) to the initial length of the sample. As for true strain which applies nominal (fully langrangian) definition, we relate the elongation to the reduction in the local width of the sample using transverse isotropy assumption and use incompressibility assumption to formulate width-based elongation (Eq. (3)). This is the same local region where the retardation measurements are made. For Hencky strain, we use the logarithmic definition of width-based strain measurements (Eq. (4)). Throughout this paper, we will use Hencky strain as it is this definition that is coupled to true stress through deformation energy up to large strains.

Following the Cauchy definition, true stress (Eq. (4)) is calculated by dividing instantaneous force measured by a load cell with the instantaneous cross-sectional area using real time width measurement and transverse isotropy (Eq. (2)).

Table 1
Compositions and average molecular weights of polyetherurethanes obtained by the stoichiometric reactions between CHDI and PTMO.

Polymer code	PTMO $\langle M_n \rangle$ (g/mol)	HS content[a] (wt%)	Polymer $\langle M_n \rangle$ (g/mol)	Polymer $\langle M_w \rangle$ (g/mol)	PDI (M_w/M_n)
CHDI-1U	1020	14.0	48,000	73,000	1.52
CHDI-2U	2040	7.5	57,000	94,000	1.65

[a] Hard segment (HS) content is the weight percent of diisocyanate in the polymer calculated from the stoichiometry of the reaction.

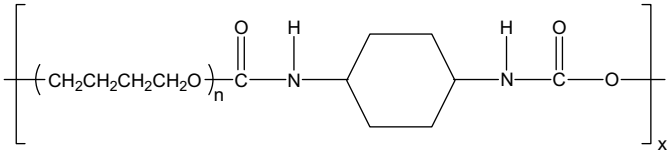

Fig. 1. Chemical structure of CHDI and PTMO-based polyurethanes (PTMO1k $n = 14$, PTMO-2k $n = 28$).

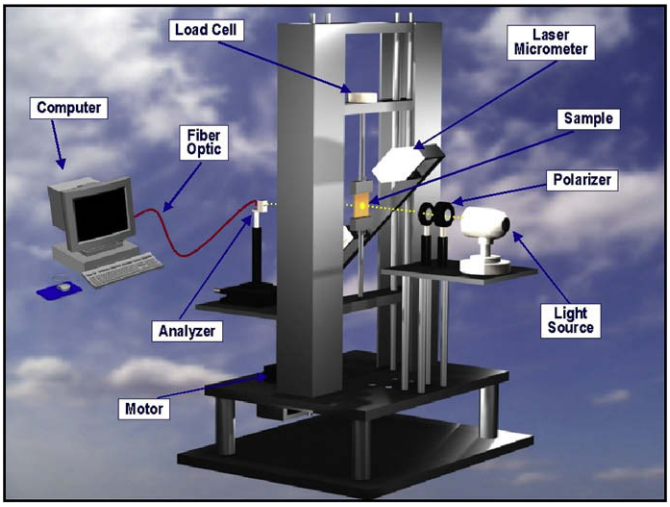

Fig. 2. Spectral birefringence stretching machine.

These relationships and the derivations are shown below.

$$W_t/W_o = D_t/D_o \quad (1)$$

$$D_oW_oL_o = D_tW_tL_t \quad (2)$$

$$\text{True strain} = \frac{\text{Elongation}}{\text{Initial length}} = \frac{L_t - L_o}{L_o} = \frac{\Delta L}{L_o} = \left(\frac{W_o}{W_t}\right)^2 - 1 \quad (3)$$

$$\text{Hencky strain} = Ln\left(\frac{L_t}{L_o}\right) = Ln\left(\frac{W_o}{W_t}\right)^2 \quad (4)$$

$$\text{True stress} = \frac{\text{Force}}{\text{Cross sectional area}} = \frac{F_t}{W_tD_t} = \frac{F_t}{\left[\left(W_t^2/W_o\right)D_o\right]} \quad (5)$$

where

W_t: real time width of the film
W_o: initial width of the film
D_o: initial film thickness
D_t: real time film thickness
L_o: initial length of the film
L_t: real time length of the film
F_t: force

Samples for stretching were prepared by cutting the cast films into dumbbell shaped specimens of 25 mm and a length of 30 mm. The initial thickness of each sample and length was measured using a precision thickness gauge prior to stretching and entered in the stretching program. Extra caution was exercised not to compress the elastic and soft polyurethane samples during thickness measurements. All the stretching experiments were performed at room temperature.

After stretching is complete, the mid-portion of the stretched samples was securely clamped between the two metal rectangular frames (thickness ~4 mm) that are held together by four screws at the corners (Fig. 3). With the help of serrated surfaces facing the stretched samples, these clamps prevented any possibility of slippage during offline characterization experiments.

2.3.5. Wide angle X-ray diffraction (WAXS) and small angle X-ray scattering (SAXS)

A Bruker AXS X-ray generator equipped with a two-dimensional wire detector was used to acquire 2D WAXS patterns. The generator was operated at 40 KV and 40 mA and the collimated X-ray beam was monochromatized to CuKα radiation. As-cast (unstretched) films as well as samples stretched to a series of deformation levels were analyzed.

SAXS patterns were obtained using S-Max3000 Rigaku SAXS system. As in WAXS experiments, the samples were exposed to X-ray in their as-cast (unstretched) and stretched forms with the beam directed along the thickness (normal) direction. The long spacing, L, measured along q ($4\pi\sin\theta/\lambda$), of the samples was obtained from the peak position of $I(q)$ according to Bragg's law: $L = 2p/q_{max}$.

2.3.6. Atomic force microscopy

Both as-cast and stretched samples were used in AFM experiments. The height and phase images were obtained by using a Nanoscope III Multimode microscope from Digital Instruments operating in the tapping mode with aluminum-coated AFM probe (Nanosensors™ PPP-NCHR, length 125 μm, width 30 μm, thickness 4 μm, 330 kHz frequency). As-cast polyurethane films were used directly for AFM experiments without any treatment including annealing. For stretched samples, a special AFM clamp was designed to preserve the sample in desired stretched state and inserted in AFM measuring head.

3. Results and discussion

3.1. Structure of as-cast films

Wide variety of structures has been proposed for polyurethanes and it is generally accepted that both the soft and the hard segment can be semicrystalline or completely amorphous depending on the chemical architecture of the polymer. Typically, the glass transition temperature of the soft segments is well below the room temperature (−50 to −120 °C) and that of the hard segments is usually around 100 °C, where hydrogen bonds start dissociating. The melting of crystalline soft segment typically occurs around room temperature and the hard segments melt around 150 °C or above depending on its chemical structure, segment length and structural order.

DSC cooling and heating thermograms are shown in Figs. 4 and 5 for CHDI-1k and CHDI-2k, respectively. The TPUs synthesized in this study have quite low-hard segment content resulting in 14.0 and 7.5% by weight urethane hard segment content for CHDI-1U and CHDI-2U, respectively. The urethane hard segment length in our polymers is very uniform but also very short, equal to the length of the diisocyanate. Therefore, well-ordered microcrystalline

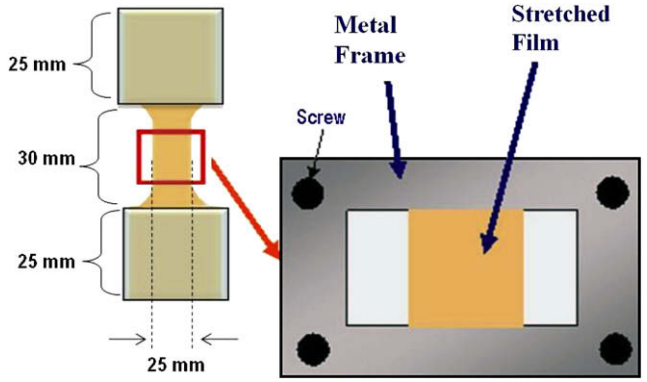

Fig. 3. Stretched film clamping mechanism for offline characterization experiments.

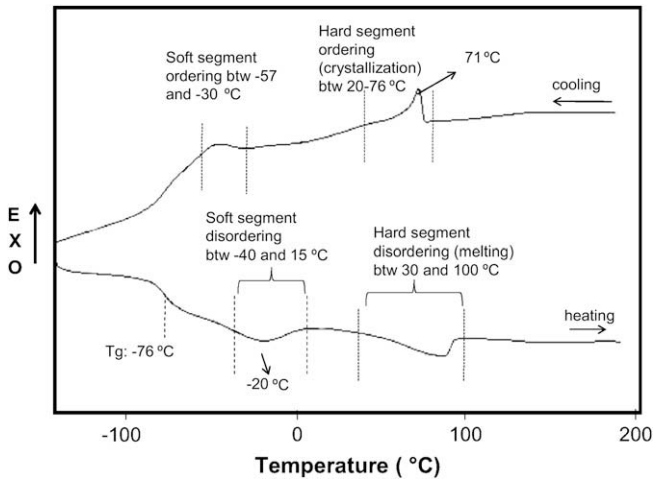

Fig. 4. DSC cooling and heating thermograms of CHDI-1U (PTMO1k $n = 14$).

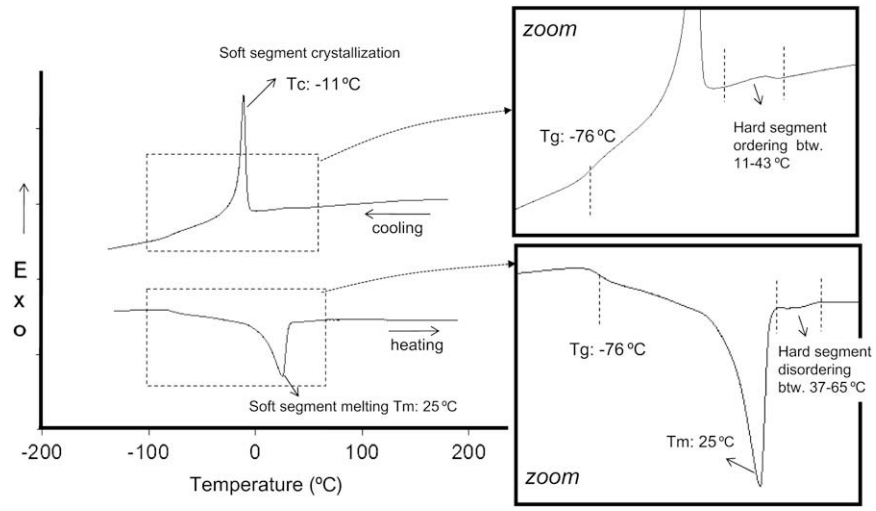

Fig. 5. DSC cooling and heating thermograms of CHDI-2U (PTMO-2k $n = 28$).

regions with long-range order could not form in either CHDI-1U or CHDI-2U, which explains the absence of a high temperature melting endotherm (>200 °C) in our DSC thermograms. Instead, a fairly broad endotherm between 30 and 100 °C is observed in CHDI-1U in Fig. 4 heating cycle, which is attributed to the disordering of its small amount of hard segments that posses short range order. It was previously shown that the disordering of hard segments with short range order could also occur between 120 and 170 °C when the hard segment content is higher and/or their chains are longer [29,46]. When the hard segments are sufficiently long, this short range order can be reorganized into well-ordered microcrystalline regions which melt above 200 °C [47]. The broad ordering (crystallization) exotherm that corresponds to the hard segment disordering endotherm between 30 and 100 °C is observed at temperatures between 20 and 76 °C. The softer grade CHDI-2U contains 7 wt% hard segments. Detailed analysis of its DSC reveals that it still exhibits ordering and disordering in the zoomed view of the data shown in Fig. 5.

In Fig. 6, we show the broad hard segment disordering (melting) endotherm of the hard grade CHDI-1U samples that were subjected to three different thermal history. The broad melting endotherm between 30 and 100 °C is in fact an unstable double peak endotherm which is clearly influenced by the cooling prehistory.

Having established the nature of hard segment order–disorder behavior, we now focus on the soft segment order–disorder transitions in DSC. In Fig. 5, we observe a sharp crystallization exotherm at Tc: −11 °C and melting endotherm Tm: 25 °C corresponding to CHDI-2U soft segments. The longer soft segment chain length in CHDI-2U facilitates their crystallization. In the polymer that has shorter soft segments, CHDI-1U, this crystallization is absent pointing to a critical soft segment length below which thermally activated crystallization is not possible (Fig. 4).

As for the glass transition temperatures, both CHDI-1U and CHDI-2U (in Figs. 4 and 5 respectively) exhibit the same soft segment glass transition temperature at −76 °C. This Tg is close to the Tg of the virgin PTMO oligomer [48,49] indicating that there is little or no mixing of hard and soft phases [20].

Fig. 7 shows the AFM phase image of as-cast CHDI-1U film. The hard segments appear as bright lines in the phase image. This

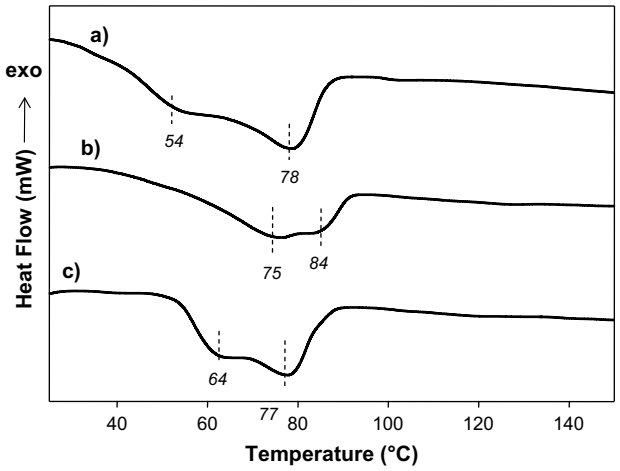

Fig. 6. Disordering (melting) endotherm of hard segments exposed different thermal history. a) 1st run – heating from room temperature. b) 2nd run – heating after fast cooling @ ~100 °C/min to −150 °C. c) 3rd run – heating after annealing at 60 °C for 4 h.

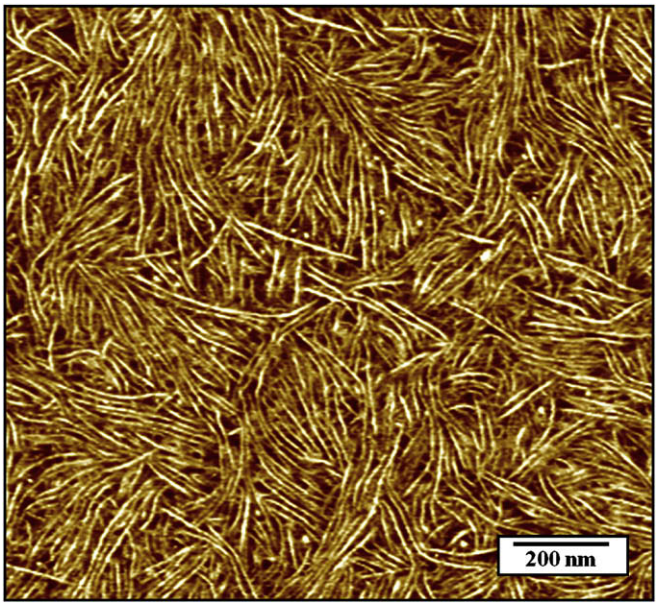

Fig. 7. AFM phase image of CHDI-1U showing the evidence of a microphase separated structure with hard segments.

morphology is clearly one of interwoven network of hard and soft segments. Fig. 8 shows the long spacing (hard segment + soft segment thicknesses) calculated from SAXS for hard grade CHDI-1U and soft grade CHDI-2U. Long spacing increases from 8.5 nm to 12 nm when the soft segment molecular weight is increased from 1020 to 2040 g/mol.

3.2. Mechano-optical behavior during uniaxial stretching

The real time monitoring of coupled mechanical and birefringence measurements eliminates potential temporal changes that take place during offline measurements. Our main studies were carried out using a special stretching machine that measures the real time true stress, true strain and birefringence simultaneously during deformation and holding. The Hencky stress–strain data using the special stretching machine in Fig. 9 reveals that the CHDI-1U exhibits higher modulus, which is expected due to its higher hard segment content, and onset of strain hardening (point C) on this material appears at lower strain. Following the deformation, holding stage indicated a small increase in strain accompanies the stress relaxation. As reference, however, we also provide standard tensile test data in Table 2 for both materials. Both materials exhibit high ultimate tensile strength (~25 MPa) and elongation to break (~1000%). The modulus of CHDI-1U (60 MPa) is six times larger than that of the CHDI-2U (10 MPa) due to the difference in the hard segment content.

In order to identify the structural deformation mechanisms taking place during stretching of a polymer, it is helpful to establish the relationships between its birefringence and the mechanical parameters (e.g. stress, strain). With our stretching machine and integrated optical set-up, we were able to identify and quantify the structural transitions as reflected in the mechanical responses.

Fig. 10 shows the birefringence vs. true stress profiles for CHDI-1U and CHDI-2U stretched to low as well as high strains followed by relaxation in their constrained states for 20 min. The CHDI-1U with shorter PTMO exhibits much longer initial linear stress optical behavior as compared to CHDI-2U. Beyond this initial region, rapid series of non-linear region are observed before birefringence begins to level off. The birefringence behavior during the holding stage following a series of deformation exhibits distinct behavior for the two grades, i.e. CHDI-1U and CHDI-2U. For the harder grade, CHDI-1U, during the holding stage, birefringence remains almost constant, whereas the stress relaxes

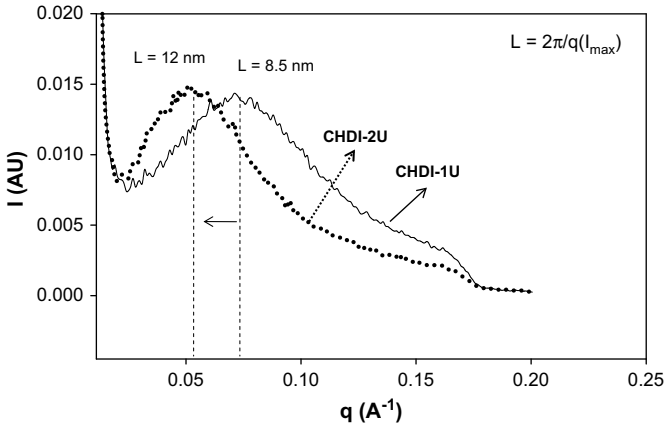

Fig. 8. Scattering intensity vs. scattering vector from SAXS for as-cast CHDI-1U and CHDI-2U films (L: long spacing (distance between two hard segments)) b) AFM phase image CHDI-1U.

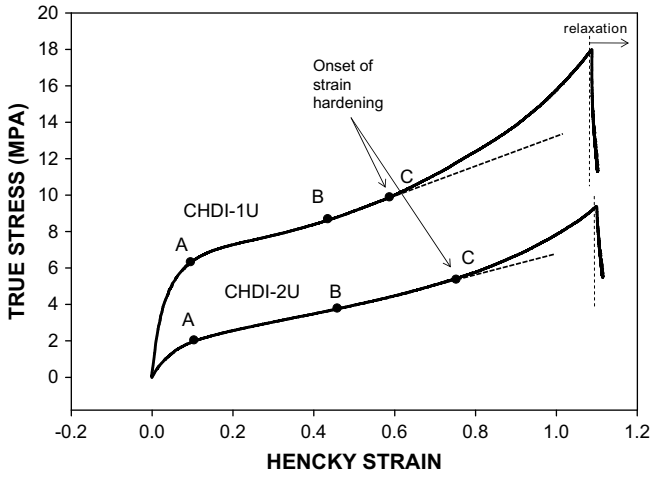

Fig. 9. True stress vs. Hencky strain curves of CHDI-1U and CHDI-2U at room temperature stretched with 20 mm/min stretching rate followed by 10 min relaxation.

significantly. This is true at both high and low levels of stretching as observed in Fig. 10 (left). Even at such low levels of stretching, birefringence never relaxes along the same stress optical path as obtained during stretching. In slow crystallizing polymers such as PET [43], PLA [50] and PEN [51] with complete initial amorphous structure in the as-cast state, after such low levels of deformation, birefringence always relaxes to zero along the same path of stretching. It is only after the onset of structural transitions either by strain-induced crystallization or some other ordering process that the network forms and birefringence increases or stays level after cessation of extension. As will be discussed in more detail below, CHDI-1U does not form a new structure or strain crystallize due to the low M_w of its soft segments. The fact that birefringence stays constant during the holding stage, especially after low levels of strain, indicates that a strongly held physical network already exists in CHDI-1U before stretching. The network is obviously that of hard segments acting as physical cross-linking sites distributed in a pool of soft segments as suggested earlier [23–25]. A similar behavior is seen in the case of PVC during holding at constrained state following small deformation where the birefringence stays nearly constant [52] or decreases very slightly while the stress relaxes substantially. In the case of PVC, the strongly connected network is formed by a small amount of widely distributed PVC crystallites acting as network junctions [53,54] in an amorphous pool of chains.

The plot in Fig. 10 (right) shows that unlike the harder grade, the soft grade CHDI-2U displays increasing levels of birefringence during holding at high strains (eng strain 1.8 and 4 while Hencky strain 0.77 and 1.09 respectively) while the stress relaxes. This increase in birefringence during relaxation is attributed to the strain-induced crystallization of the soft segments in CHDI-2U. The soft segment M_w is twice as high in CHDI-2U which renders the soft segment chains crystallizable with strain. Supporting evidence for strain-induced crystallization in CHDI-2U is given below. It is also evident that strain-induced crystallization does not start at low

Table 2
Room temperature stress–strain properties of CHDI-based PTMO-urethanes.

Polymer code	PTMO ⟨M_n⟩	HS (wt%)	Modulus[a] (MPa)	Ultimate tensile strength[a] (MPa)	Elongation[a] (%)
CHDI-1U	1020	14.0	60	23	950
CHDI-2U	2040	7.5	10	26	1050

[a] Measured by traditional tensile testing.

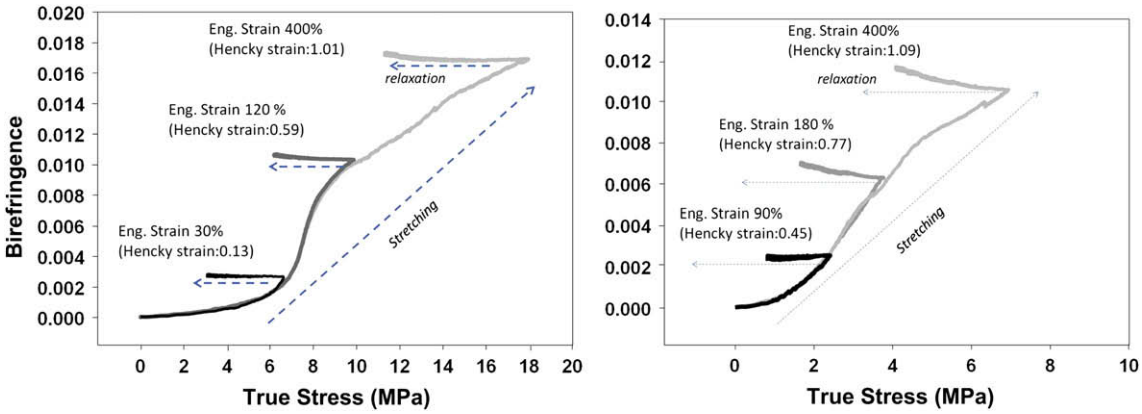

Fig. 10. Birefringence vs. true stress for CHDI-1U (left) and CHDI-2U (right).

levels of strain (eng. strain 0.9 Hencky strain 0.45) where the slope of the relaxation curve, i.e. birefringence/stress, stays constant. One can notice from these relaxation curves that birefringence is not necessarily a function of stress and can remain constant or even increase while the stress is decreasing as a result of crystallization [55].

Birefringence is plotted against true stress and Hencky strain in Fig. 11 along with SAXS and WAXD patterns at various levels of extension. We identify three critical points marked as A, B and C on these curves. Point A is the end point of the initial stress plateau region in the birefringence–true stress curve where the onset of steep birefringence rise with stress starts. This is also the point where the yielding takes place in the true stress vs. Hencky strain curve (Fig. 9). In fact, one can notice that the birefringence vs. true stress curve resembles roughly an inverted true stress vs. Hencky strain curve (Fig. 9) since birefringence is a reflection of molecular strain whereas Hencky strain is a macro level strain. Both SAXS and WAXD patterns exhibit isotropic patterns for the hard segment phase at point A. This clearly indicates the main structural reorganization responsible for this initial small birefringence rise in this stage up to point A is attributable to the orientation of the soft segments. Between A and B, a mild anisotropy develops in the SAXS and WAXD patterns. The scattering in SAXS represents the typical long-range correlation of the hard segment domains. Excellent contrast is achieved in SAXS due to the electron density difference between the hard and soft segments. The anisotropy that develops in the WAXD patterns in Fig. 11 is due to the strain-induced orientation of the hard segments. Multiple peaks of soft segment strain-induced crystallization was reported for PTMO–MDI polyurethane urea with a M_w of 1800 for PTMO and the peak around $2\theta = 19.7^\circ$ was attributed in this case to the (110) strain-induced crystals of PTMO [38]. However, we assign the reflection at $2\theta = 20.3^\circ$ and d-spacing 4.4 Å in our WAXD patterns to the strain-induced orientation of the hard segment and not to the strain-induced crystallization of the soft segments. First reason is that the M_w of our soft segments in CHDI-1U is too short (1020) to crystallize by strain. Others reported the absence of strain-induced crystallization for a low-hard segment content polyurethane urea synthesized with low-molecular weight PTMO soft segments (M_w 350 and 1100) and Bis(ureido)buthylene hard segments without chain extender as well [12]. In this case, the WAXD reflection at $2\theta = 19.7^\circ$ and d-spacing 4.64 Å was attributed to the urea bifurcated hydrogen bonding motif with a urea–urea distance of 4.64 Å. Our d-spacing value of 4.4 Å points to a similar spacing most likely between the hydrogen bonded urethane groups. In addition, when one compares the WAXD pattern of CHDI-1U (Fig. 11) and CHDI-2U (Fig. 14) at a Hencky strain of ~0.6, one can see that the anisotropic reflection at $2\theta = 20.3^\circ$ has not developed in the softer grade

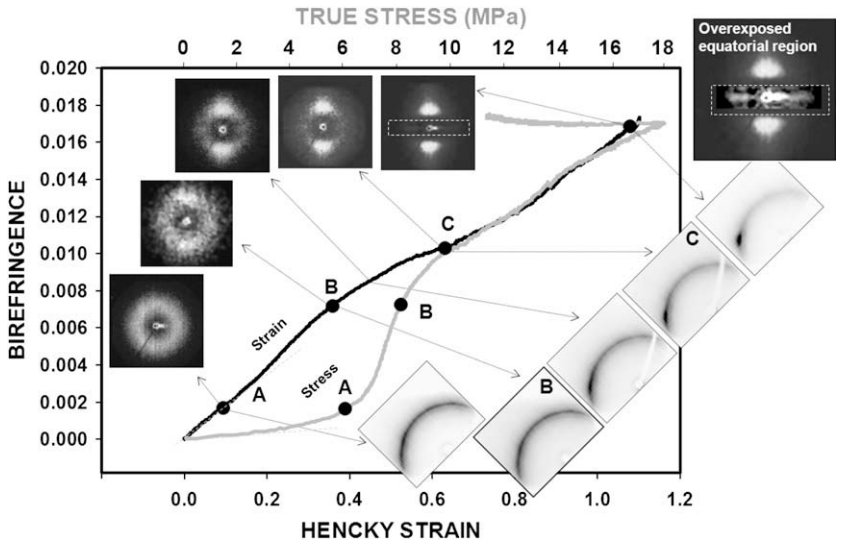

Fig. 11. Birefringence vs. Hencky strain of CHDI-1U film during stretching at 200 mm/min up to a stretch ratio of 5×.

CHDI-2U (Fig. 14) in spite of the ability of soft segments to strain crystallize substantially in this grade due to its higher M_w (2040). In fact, the reflection is less pronounced probably due to the lower content of hard segments. Lastly, perhaps more indirect, the evolution of anisotropy in SAXS and WAXD reflection is very similar indicating that it belongs to the same phase. No indication of strain crystallization is seen in SAXS patterns for CHDI-1U at a Hencky strain of 0.6. Inability to thermally crystallize was evidenced by DSC as well although this does not include the effect of strain. Therefore, we attribute this reflection in the WAXS to oriented hard segments. Although birefringence could include contributions from both the soft and the hard segments, the birefringence increase between points A and B in CHDI-1U is primarily attributed to the orientation of the soft segments since the hard segment content is low and the hard segment orientation as evidenced from SAXS and WAXD at this level of strain is very small. Comparing the strain optical data with stress optical data, the linear strain optical path before point B is highly non-linear in the stress optical data. At point B, a negative deviation of birefringence from the initial linear strain optical regime is noted. Between points B and C, the hard segments rotate and orient with their long axes perpendicular to the stretching direction as evidenced by SAXS and WAXD. The rotation and orientation of the hard segments occur quickly in this transition zone since the population of soft segment chains, which are already stretched substantially at point B, start to pull the hard segments and cause them to align perpendicular to the stretching direction. This translates into a negative slope change for both the birefringence true strain and birefringence true stress curves. The stretched soft segments now do not orient as readily since they are pulling on the hard segments. Birefringence value in this transition zone could also have contributions from the hard segment chains orienting due to the rotating hard segment lamellar domains. If the polymer chains in the hard segment lamellar domains are positively birefringent ($n_{\parallel} > n_{\perp}$) and if the chain axis is perpendicular to the lamellar domain axis as it is typically observed for lamellar domains [56], the polymer chains would contribute positively for a lamellar domain that is in perpendicular orientation with respect to the stretching direction. Examining the CHDI structure in Fig. 1, we can consider the chain to be positively birefringent. Our SAXS patterns for CHDI-1U indicate a gradual increase of scattering intensity in the meridian forming a two-point pattern indicative of gradual rotation of the lamellae perpendicular to the stretching direction. During the course of this rotation, a four-point SAXS pattern from tilted lamellae, observed for some polyurethane systems during the course of stretching [38,39] does not occur. The fact that we see a negative deviation in birefringence despite parallel hard segment chain orientation in lamellar domains in normal orientation to the stretching indicates that the decrease in birefringence is due to the effect of that population of soft segments that are reaching a threshold extension and start pulling on the hard segments causing their rotation. The orientation of the hard phases normal to the stretching direction after point B is also evidenced directly by AFM phase images in Fig. 12. At higher strains in Fig. 11, to be more precise at 500% gauge separation corresponding to a width-based Hencky strain of about 1.01, breakdown of the hard segment lamellae is observed by the presence of a streak in a highly overexposed and image enhanced equatorial region of the SAXS pattern. One can notice from the original SAXS pattern that the streak pattern is in fact quite low in intensity due to its low concentration. Breakdown of the hard segment lamellae forming nanofibrils in the stretching direction and scattering as a streak pattern in the equator was noted earlier [38,39,57]. These nanofibrils were also shown to contain strain-induced soft segment crystals. However, as discussed above,

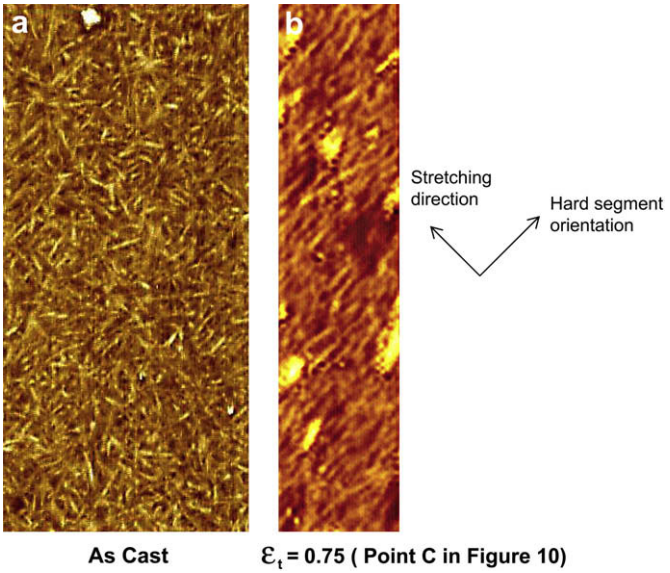

Fig. 12. AFM phase images of a) as-cast and b) stretched CHDI-1U film at a true strain value of 0.75 (point C in Fig. 10) (No post treatment).

strain-induced crystallization of soft segments is not present in the hard grade CHDI-1U and therefore the faint equatorial streak is entirely attributed to nanofibrils formed by the broken down hard segments. In fact, as will be apparent in the birefringence vs. Hencky strain of the softer grade in Fig. 14, this equatorial streak is much more intense and starts forming much earlier pointing to strain-induced crystallization of the soft segments.

The long-spacing values, i.e. the distance covering one soft segment region and one hard segment region, was calculated and plotted as a function of Hencky strain in Fig. 13 for CHDI-1U. The three critical points are also placed on this graph for ease of visualization. Until point B the increase in long spacing is minimal since soft segment orientation takes place primarily in the initial stages of stretching. One can also notice from WAXD and SAXS in Regime I of Fig. 11 that the orientation of the hard domains has not developed appreciably at this point. Between B and C, the increase in long spacing is still minimal indicating that the rotation of the hard

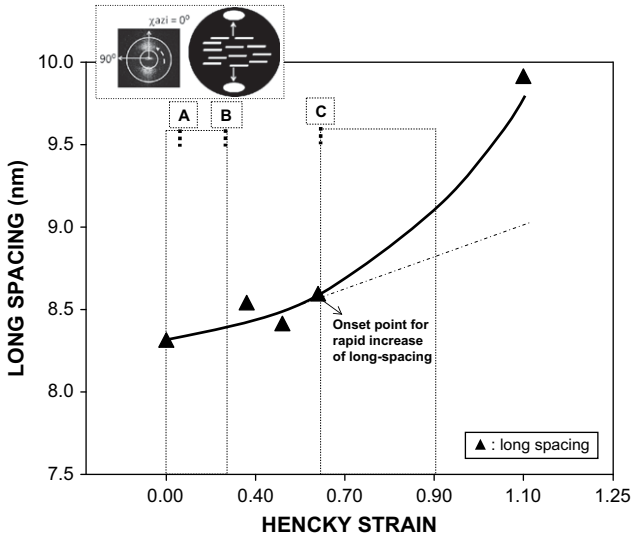

Fig. 13. Long spacing vs. Hencky strain for CHDI-1U film showing more rapid increase of long spacing after point III.

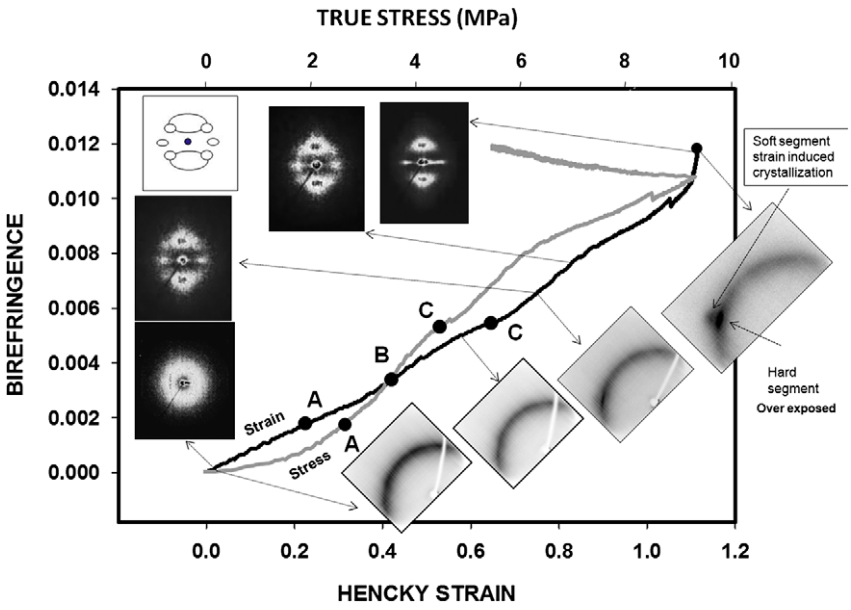

Fig. 14. Birefringence vs. Hencky strain of CHDI-2U film during stretching at 20 mm/min up to a stretch ratio of 5×.

segments is taking place without a noticeable increase in spacing between them. On the other hand, orientation of the hard segment phase increases largely after point B as evidenced from WAXS and SAXS patterns in Fig. 11. At point C, the orientation of the hard segments approaches the limit value (Fig. 11) after which a rapid increase in long spacing starts. It is interesting to note that point C, which corresponds to the onset of rapid long spacing increase in Fig. 13, also corresponds to the onset of strain hardening in the true stress and Hencky strain curves provided in Fig. 9. This is because the structural transitions that the phases are going through beyond point C involves breaking of the extended nanofibrils from the hard segment lamellae that are separating, i.e. long spacing increasing, and this requires more stress than that required for structural processes before point C, i.e. extension of the soft segment chains and rotation of the hard segments. However, this strain hardening is observed at quite low levels, i.e. at around 120% elongation. This sample exhibits elongation to break values up to 1000%.

Fig. 14 shows the birefringence vs. Hencky strain along with the X-ray patterns for the softer grade polyurethane system, CHDI-2U. As discussed above, the softer grade CHDI-2U, exhibits strain-induced crystallization as evidenced by the presence of the equatorial peaks in the SAXS patterns. It is well-known that molecular orientation of polymer chains changes the driving force and even the mechanism of crystal growth. Molecular orientation decreases the entropy which in turn increases the melting temperature of the polymers [58]. The increase in melting temperature brings the system to a supercooled state that leads to high nucleation rates of extended chain segments and their growth as shish structures (nanofibrils) in the direction of stretching. The first detection of strain-induced crystallization is observed well after substantial development in birefringence, i.e. ~0.005, after point C. At this point, the elongation is 280% corresponding to about 0.77 width-based Hencky strain. As we have seen in Fig. 10, crystallization in CHDI-2U is marked by increasing birefringence as soon as the stretching comes to a halt and the stress is relaxing. As Flory suggested, a certain amount of relaxation is necessary to crystallize oriented structures [58] and it could very well be that the crystallization for the most part occurs during relaxation. Strain crystallization during stretching could also take place, especially if the rate of stretching is low enough to allow partial relaxation of the chains. One can see that the equatorial SAXS signal first appears point like on the equator and then smears with a very narrow width indicating that in real space they resemble needle-like nanofibrillar crystals arranged in the stretching direction with some degree of variability in their lateral periodicities. Along with the equatorial signal, careful examination reveals a faint four-point pattern partially superimposed on the meridional two-point signals. In order to clarify the pattern, we have also provided a sketch of this pattern. The faint four-point pattern disappears at further strains. These were previously shown to originate from a small amount of tilted hard segment lamellae which disappears with further stretching [38,39]. Fig. 15 shows the nature of the WAXD and SAXS patterns in more detail for a sample stretched substantially to a Hencky strain value of 1.5 (percent elongation 700%). One can clearly see the signals coming from the hard and soft segments individually in both WAXS and SAXS patterns. In order to assess whether void formation is a possibility, we have analyzed radial (long spacing) and azimuthal profiles. It is apparent that the radial intensity profile goes through a maximum and intensity decays to zero in the vicinity of the beam stop. This is not common in air trapped void scattering. The azimuthal intensity profile shows that the intensity of the soft segment crystals is lower than hard segments. Air trapped voids would show much higher scattering intensities. All these findings indicate that void formation does not play a role in these patterns. The WAXD pattern shown in Fig. 15a identifies the peaks corresponding to hard segments and soft segments. They exhibit near perfect orientation and each of these phases lack translational order along their chain axes as evidenced by the absence of off-equatorial crystalline peaks. In addition, the diffraction peak for the soft segment is broader as compared to the hard segments indicating the lateral packing in soft segment regions is not as good as the hard segment regions. We also note that the amorphous halo still exhibits considerable isotropy in this pattern as well as in prior WAXD patterns in Figs. 11 and 14, attesting to the fact that there is still an appreciable amount of disoriented amorphous phase present in the structure even at high strains. This is very similar to that seen in highly stretched natural rubber WAXD patterns where an isotropic amorphous halo is superimposed on highly oriented intense crystalline reflections [59–61]. Only those amorphous rubber chains that are linked

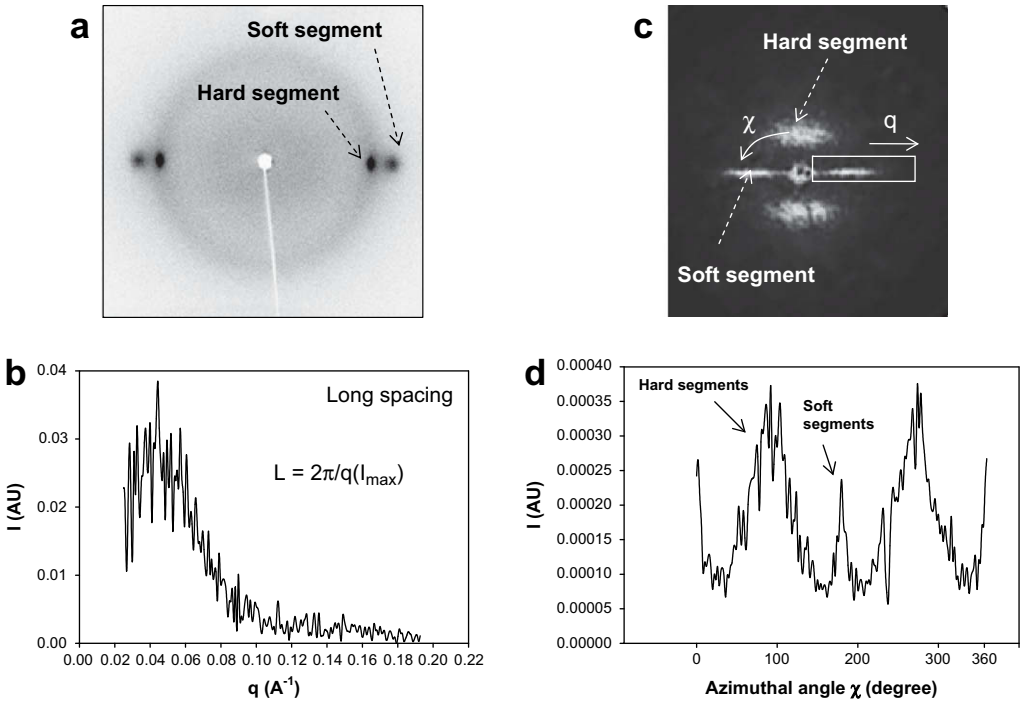

Fig. 15. CHDI-2U stretched to a Hencky strain value of 1.4. a) WAXD pattern. b) 2D SAXS pattern. c) Scattering intensity vs. scattering vector from 2D SAXS pattern in (b). d) Azimuthal intensity profile of (b).

through cross-links are susceptible to orientation and responsible for the early development of birefringence. It was further shown that some of the fatty acids located at the ends of some of the natural rubber chains [62] were integrated with the cross-linked natural rubber network and become oriented from very early stages of deformation before the appearance of the crystalline peaks from the rubber phase [60]. A similar analogy can be made where not all of the soft segment chains are directly linked to the cross-linking hard segments. Vast majority of chains that are not part of the network remain unoriented or perhaps relax during the course of stretching.

Comparing Fig. 16 with Fig. 13, the long spacing values of CHDI-2U are about 3 nm larger than that of the harder grade CHDI-1U at all strains due to longer chain length of the segments. Therefore, it spans a larger distance to stretch the soft segments fully in between the points A and B and hence the occurrence of point C, onset of strain hardening point, is delayed in the entire stretching process.

3.2.1. Summary

Based on the above findings, we identify multiple mechano-optical regimes shown in Fig. 17 on birefringence–Hencky strain curves for both grades of polyurethanes along with the corresponding models. At low deformation levels, both materials exhibit linear strain optical behavior with the CHDI-2U showing smaller strain optical constant (compare linear Regime I of CHDI-1U and CHDI-2U in Fig. 17). In this regime, birefringence increase is due to the orientation of certain population of soft segments linked to the network. Following this linear regime (Regime I), a negative deviation is observed. In this transition the rotation of the hard segment domains takes place causing a negative deviation from the linear Regime I. Beyond Regime II, Regime III starts with a slight negative deviation and continues with a constant slope. Regime III is primarily influenced by the broken nanofibrils in CHDI-1U and strain-induced crystallites in CHDI-2U. Following Regime III, the sample deformation is halted and a considerable increase in birefringence due to strain-induced crystallization is observed for CHDI-2U during the relaxation stage while the birefringence stays constant for CHDI-1U.

The models include components from hard segments, nanofibrils from broken down hard segments, unoriented and oriented soft segment chains and strain crystallized soft segment chains for CHDI-2U. The models indicate that initially the network is that of isotorpic hard segments distributed in a pool of unoriented amorphous soft segment phase. With strain, those soft segments chains that are cross-linked to the hard segment lamellae orient and subsequently cause the rotation of the lamellae transverse to the stretching direction and start increasing their long spacing distance. At higher strains, nanofibrils from broken down hard phase also form. The model also shows that a considerable amount

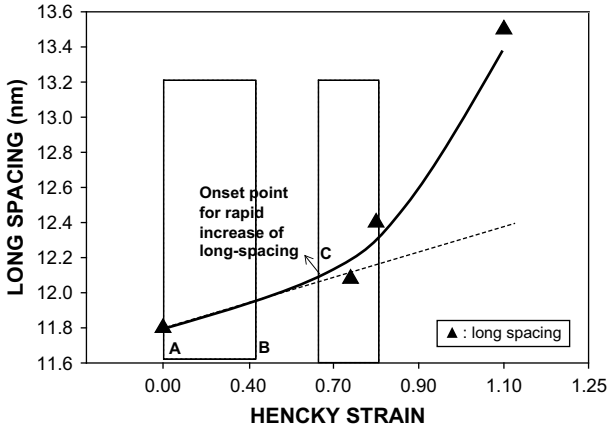

Fig. 16. Long spacing vs. Hencky strain for CHDI-2U film showing more rapid increase of long spacing after point III.

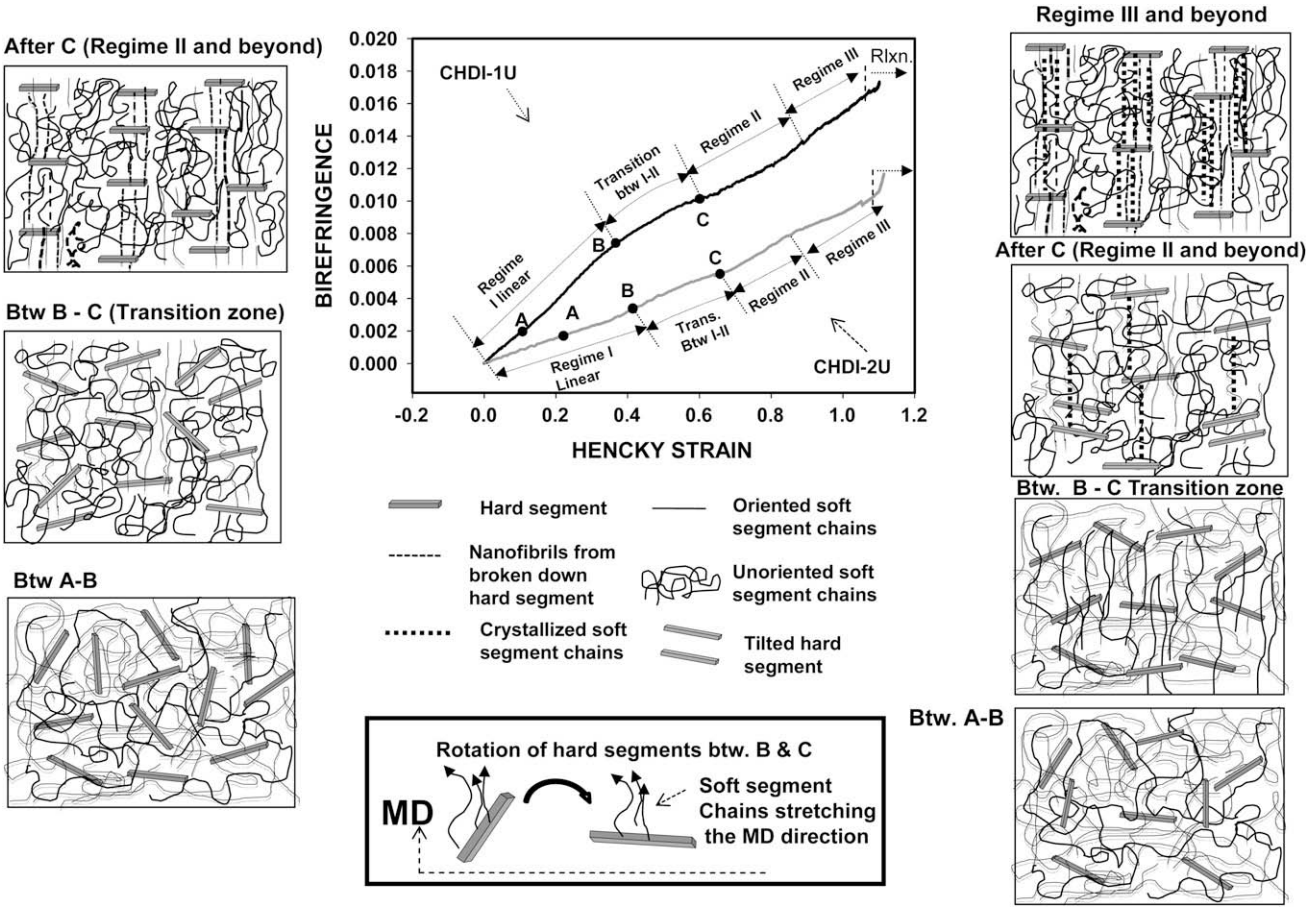

Fig. 17. Model depicting the stretching behavior in the hard (CHDI-1U left column) and soft grade (CHDI-2U right column). The cartoons are not to scale and do not represent actual morphology. Each drawn lamella represents a stack.

of unoriented amorphous phase is still present at these high strains. The softer CHDI-2U, unlike the harder CHDI-1U, exhibits strain-induced crystallization of soft segments primarily in Regime II after point C.

4. Conclusions

The phase behavior of novel, non-chain extended, high strength, segmented polyurethanes synthesized based on stoichiometric reactions of trans-1,4-cyclohexyl diisocyanate and poly(tetramethylene oxide)glycol oligomers with $\langle M_n \rangle$ values 1020 (CHDI-1U) and 2040 g/mol (CHDI-2U) were investigated. These polyurethanes have quite unique multi-stage strain and stress optical behavior. The mechano-optical behavior together with our structural analysis revealed that in the first linear strain optical regime (Regime I), certain population of soft segments begin to orient (a behavior analogous to the cross-linked rubber systems). At the end of this Regime I, we clearly observe that these soft segments begin to "tug" on the connected hard segments which rapidly undergo reorientation with their chain axes in the stretching direction while the long axes of these hard segment domains align normal to the stretching direction. This appears to be network-tightening process and signals the transition from Regime I, where high-strain optical constant was observed, to Regime II where lower strain optical regime is observed. In Regime II, the increase in birefringence comes from further extension of these soft segment linkages between the hard segments that may also involve straining of the bonds. In CHDI-1U nanofibrils form from broken down hard segments at high strains whereas CHDI-2U that contains longer soft segments exhibits strain-induced crystallization. CHDI-1U having shorter soft segments does not strain crystallize suggesting that there is a critical soft segment length beyond which strain-induced crystallization can take place.

References

[1] Schollenberger CS. Thermoplastic polyurethane elastomers. In: Handbook of elastomers. New York: Marcel Dekker Inc.; 2001. p. 387.
[2] Hepburn C. Polyurethane elastomers. Essex, UK: Elsevier Science Publishers Ltd; 1992.
[3] Burke A, Hasirci N. Adv Exp Med Biol 2004;553:83–101.
[4] Guan JJ, Wagner WR. Biomacromolecules 2005;6(5):2833–42.
[5] Santerre JP, Woodhouse K, Laroche G, Labrow RS. Biomaterials 2005; 26(35):7457–70.
[6] Demirbas U, Kurt A, Sennaroglu A, Yilgor E, Yilgor I. Polymer 2006;47:982–90.
[7] Lendlein A, Langer R. Science 2002;296(5573):1673–6.
[8] Ping P, Wang W, Chen X, Jing X. Biomacromolecules 2005;6(2):587–92.
[9] Chen WC, Chen HH, Wen TC, Digar M, Gopalan AJ. Appl Polym Sci 2004;91(2):1154–67.
[10] Koevoets RA, Versteegen RM, Kooijman H, Spek AL, Sijbesma RP, Meijer EW. J Am Chem Soc 2005;127:2999–3003.
[11] Makal U, Uilk J, Kurt P, Cooke RS, Wynne KJ. Polymer 2005;46(8):2522–30; Makal U, Fujiwara T, Cooke RS, Wynne KJ. Langmuir 2005;21(23):10749–55.
[12] Versteegen RM, Kleppinger R, Sijbesma RP, Meijer EW. Macromolecules 2006;39:772–83.
[13] Lelah MD, Cooper SL. Polyurethanes in medicine. Boca Raton, FL: CRC Press; 1986.
[14] Abouzahr S, Wilkes GL. In: Folkes MJ, editor. Processing, structure and properties of block copolymers. London: Elsevier Applied Science Publishers; 1985. p. 165–207.
[15] Sheth JP, Klinedinst DB, Wilkes GL, Yilgor I, Yilgor E. Polymer 2005;46(18): 7317–22.

[16] Yilgor I, Yilgor E. Polym Rev 2007;47(4):487–510.
[17] Das S, Klinedinst DB, Yilgor I, Yilgor E, Beyer FL, Cox DF, et al. J Macromol Sci Part B Phys 2007;46(5):853–75.
[18] Das S, Yilgor I, Yilgor E, Inci B, Tezgel O, Beyer FL, et al. Polymer 2007; 48(1):290–301.
[19] Klinedinst DB, Sheth JP, Yilgor E, Yilgor I, Beyer FL, Wilkes GL. J Rubber Chem Tech 2005;78(5):737–53.
[20] Versteegen RM, Sijbesma RP, Meijer EW. Macromolecules 2005;38:3176–84.
[21] Rinke H. Angew Chem 1962;74:612.
[22] Oertel H. Textil-Praxis 1964;19:820.
[23] Cooper SL, Tobolsky AV. J Appl Polym Sci 1966;10:1837.
[24] Bonart RJ. Macromol Sci Phys 1968;2:115.
[25] Bonart R, Morbitzer L, Hentze G. J Macromol Sci Phys 1969;3:337.
[26] Estes GM, Seymour RW, Huh DS, Cooper SL. Polym Eng Sci 1969;9(6):383–7.
[27] Seymour RW, Estes GM, Huh DS, Cooper SL. J Polym Sci Part A 1972; 10:1521–7.
[28] Estes GM, Seymour RW, Cooper SL. Macromolecules 1971;4:456.
[29] Seymour RW, Allegrezza Jr AE, Cooper SL. Macromolecules 1973;6:896.
[30] Allegrezza Jr AE, Seymour RW, Ng HN, Cooper SL. Polymer 1974;15:433.
[31] Desper CR, Schneider NS. In: Frisch K, Klemper D, editors. Polymer alloys III. New York: Plenum Press; 1983. p. 233–51.
[32] Desper CR, Schneider NS, Jasinski JP, Lin JS. Macromolecules 1985;18:2755.
[33] Lin SB, Hwang KS, Tsay SY, Cooper SL. Colloid Polym Sci 1984;262:1.
[34] Siesler HW, Ber B-G. Phys Chem 1988;92:641.
[35] Kornfield JA, Spiess HW, Nefzger H, Hayen H, Eisenbach CD. Macromolecules 1991;29:4787.
[36] Reynolds N, Spiess HW, Hayen H, Nefzger H, Eisenbach CD. Macromol Chem Phys 1994;195:2855.
[37] Wang H, Graff DK, Schoonover JR, Palmer RA. Appl Spectrosc 1999;53:687.
[38] Yeh F, Hsiao BS, Sauer BB, Michel S, Siesler HW. Macromolecules 2003; 36(6):1940–54.
[39] Sauer BB, MClean RS, Brill DJ, Londono DJ. J Polym Sci Part B Polym Phys 2002;40:1727–40.
[40] Blundell DJ, Eeckhaut G, Fuller W, Mahendrasingham A, Martin C. Polymer 2002;43:5197–207.
[41] Blundell DJ, Eeckhaut G, Fuller W, Mahendrasingham A, Martin C. J Macromol Sci Part B Phys 2004;B43(1):125–42.
[42] Curgul S, Yilgor I, Yilgor E, Erman B, Cakmak M. Macromolecules 2004;37(23):8676–85.
[43] Sen TZ. Dissertation. Polymer Engineering Department: University of Akron, 2002.
[44] Valladares D, Toki S, Sen TZ, Yalcin B, Cakmak M. Macromol Symp 2002; 185:149–66.
[45] Beekmans F, Posthuma de Boer A. Macromolecules 1996;29:8726.
[46] Seymour RW, Cooper SL. Macromolecules 1973;6(1):48.
[47] Seymour RW, Cooper SL. J Polym Sci Part B 1971;9:689.
[48] Dreyfuss P. Poly(tetrahydrofuran). New York: Gordon and Breach; 1982.
[49] Mark HF, Bikales NM, Overberger CG, Mengers G. Encylopedia of polymer science and engineering. 2nd ed. New York: Wiley-Interscience; 1985.
[50] Mulligan JH, Cakmak M. Macromolecules 2005;38(6):2333–44.
[51] Martins CI, Cakmak M. Polymer 2007;48(7):2109–23.
[52] Yalcin B, Cakmak M. J Polym Sci Part B Polym Phys 2005;43(724–742).
[53] Alfrey T, Wiederhorn N, Stein R, Tobolsky AV. Ind Eng Chem 1949;41:701.
[54] Summers JW, Rabinovitch EB. J Macromol Sci Phys 1981;B20:219.
[55] Bonart R. Polymer 1979;20:1389.
[56] Bonart R, Muller-Riederer G. Colloid Polym Sci 1981;259:926.
[57] McLean RS, Sauer BB. J Polym Sci Part B Polym Phys 1999;37:859.
[58] Flory PJ. J Chem Phys 1947;15:397.
[59] Tosaka M, Murakami S, Poompradub S, Kohjiya S, Toki S, Sics I, et al. Macromolecules 2004;37:3299–309.
[60] Mitchell GR. Polymer 1984;25:1562.
[61] Valladares D, Yalcin B, Cakmak M. Macromolecules 2005;38(22):9229–42.
[62] Tanaka Y, Kawara S, Tangpakdee J. Kautsch Gummi Kunst 1977;50:6.